Biosensors and Bioelectronics 176 (2021) 112943

Contents lists available at ScienceDirect

Biosensors and Bioelectronics

journal homepage: http://www.elsevier.com/locate/bios

Controllable design of a nano-bio aptasensing interface based on tetrahedral framework nucleic acids in an integrated microfluidic platform

Fulin Zhu [a], Xiaojun Bian [a], Hongcai Zhang [a], Yanli Wen [b], Qian Chen [a], Yongliang Yan [c], Liang Li [c,***], Gang Liu [b,**], Juan Yan [a,*]

[a] Laboratory of Quality and Safety Risk Assessment for Aquatic Products on Storage and Preservation (Shanghai), Ministry of Agriculture, Shanghai Engineering Research Center of Aquatic-Product Process & Preservation, College of Food Science and Technology, Shanghai Ocean University, Shanghai, 201306, China
[b] Laboratory of Biometrology, Division of Chemistry and Ionizing Radiation Measurement Technology, Shanghai Institute of Measurement and Testing Technology, Shanghai, 201203, China
[c] Biotechnology Research Institute, Chinese Academy of Agricultural Science, Beijing, 100081, China

ARTICLE INFO

Keywords:
Tetrahedral DNA nanostructure
Pathogenic microorganism
Aptasensor
Antibiotic resistance
Food safety detection

ABSTRACT

The limited reaction time and sample volume in the confined space of microfluidic devices give considerable importance to the development of more effective biosensing interfaces. Herein, the self-assembling of tetrahedral framework nucleic acids (FNAs) with controllable size on the interface of the microfluidic microchannels is studied. Compared with macroscopic turbulence control on traditional micro-structured microfluidic surface, the novel FNA-engineered microfluidic interface successfully constructs a 3D reaction space at nanoscale by raising DNA probes away from the surface. This FNA interface dramatically improves the reaction kinetics during molecular recognition due to extremely ordered orientation, configuration and density of DNA probes on the surface. Finally, the FNA-engineered interface is applied in a novel multi-functional microfluidic platform, towards a "one-stop" assay of *Escherichia coli* O157: H7 (*E. coli* O157: H7), integrating capture, release, enrichment, cell culture and antimicrobial susceptibility testing (AST). With the FNA-aptamer probe, we achieved an enhanced bacterial detecting efficiency (10 CFU/mL) plus excellent selectivity and precision. The appicability was strongly demonstrated when the biosensor was successfully applied in real samples, including the analysis of antibiotic susceptibility and minimum inhibitory concentration (MIC) of *E. coli* O157: H7 among different antibiotics. The application of FNA interface will open a wide avenue for the development of microfluidic biosensors for other pathogenic microorganisms or circulating tumor cells (CTC) simply by changing the aptamers.

1. Introduction

For decades, microfluidic biosensors were widely applied in both basic and applied investigations, especially for small-volume sample analysis, on-site test and lab-on-a-chip assay (Li et al., 2020; Ozen et al., 2020). Using the precisely controlled fluids in small volume microfluidic channel, favorable, reliable, accurate, cost effective, and easy-to-use biosensors were developed (Dittrich et al., 2006; Whitesides 2006). For most of the microfluidic integrated biosensors, an interface covered by functional capture molecules plays a critical role for the recognition and capture of the targets in the microchannels (Foley et al., 2008). However, the binding efficiency of probes on the interface remains a major challenge to the development of microfluidic biosensors, because both the volume and the recognition time are limited in the microchannels (Lynn and Dandy 2007). The follow-on staggered herringbone microstructure that generates recirculation perpendicular to the primary flow direction is perhaps the best-known answer to improve the microfluidic recognition (Stroock et al., 2002; Williams et al., 2008). Unfortunately, such mixing approaches only increase the transport of the analytes in bulk solution, but the binding efficiency between analytes and probes on the interface still remains a bottleneck of microfluidics to overcome.

The two-phase interface where the electro migration, mass transfer, energy exchange and signal conversion happen, is the most critical for

* Corresponding author.
** Corresponding author.
*** Corresponding author.
E-mail addresses: liliang@caas.cn (L. Li), liug@simt.com.cn (G. Liu), j-yan@shou.edu.cn (J. Yan).

https://doi.org/10.1016/j.bios.2020.112943
Received 20 October 2020; Received in revised form 15 December 2020; Accepted 26 December 2020
Available online 29 December 2020

better biosensing performance (Helmke and Minerick 2006; Jones et al., 2014). Well-defined 3D self-assembled "framework nucleic acids" (FNAs) have drawn considerable research attention for the development of biosensor interface (Ge et al., 2018; Wang et al., 2019; Wiraja et al., 2019; Yang et al. 2018a, 2018b), with advantages such as simple synthesis, high yield, powerful structural rigidity and capacity of multiple functionalization with high addressability (Li et al., 2009; Liu et al., 2019; Song et al., 2020). Several reported biosensors demonstrated the high programmability of FNAs on the interface, leading to well defined orientation, density and configuration of the probes (Ge et al., 2020; Lin et al., 2015; Su et al., 2019).

Inspired by these works, a novel FNA, a tetrahedral DNA nanostructure (TDN), was designed and assembled onto the surface of the microchannel. Compared with macroscopic turbulence control on traditional micro-structured microfluidic surface, the novel TDN-engineered microfluidic interface successfully constructed a 3D binding space at nanoscale by raising DNA probes away from the surface. Thus, the reaction kinetics between the targets and the capture probes was dramatically improved.

As a proof of principle, we developed a novel multi-functional microfluidic biosensor for *Escherichia coli* (*E. coli*), which is one of the most common infections encountered in clinical practice and a common disease-causing agent affecting food safety (Hermann et al., 2019; Rajapaksha et al., 2019). The main challenges of conventional pathogen detection methods and drug sensitivity tests are analysis speed, sensitivity and requirement of intricate instruments and complex operation (Bush et al., 2011; Shin et al., 2019; Xu et al., 2016). As is well known, microfluidic assay is a very promising solution for rapid and sensitive pathogen analysis (Li et al., 2019; Liu et al., 2017; Qu et al., 2017). In the work, we successfully developed an integrated "one-stop" microfluidic biosensor, adapting the joint merits of microfluidic system and FNAs for pathogens monitoring. In this platform, each of its microchannels comprises an upstream herringbone channel for bacterial capture and a downstream microcavity structure for bacterial trapping, culture and AST. Finally, this compact microfluidic device with the built-in rigid FNA-aptamer probes and microcavities achieved ultrasensitive bacterial detection, fast and reliable AST analysis. Our work complements particularly the neglected molecular recognition between "dynamic analytes" and "static capture substrates", other than most of the traditional microfluidic assays.

2. Materials and methods

2.1. Materials

All synthetic DNA primers were ordered from Sangon Biotech with sequences tabulated in Table S1. The red letters represent restriction enzyme action sites. Other materials can be found in Supporting Information (SI).

2.2. Preparation of TDNs aptasensing interface

DNA tetrahedron was constructed with four DNA strands (T1-T4, Table S1) according to the published protocol (Lin et al., 2015). Briefly, the concentrations of DNA solutions were quantified by UV–visible spectroscopy at 260 nm. Equimolar quantities of four strands (10 μM) were dissolved in TM buffer (20 mM Tris, 50 mM $MgCl_2$, pH 8.0) with final concentrations of 1 μM. The mixture was then heated at 95 °C for 10 min and cooled to 4 °C for 25 min by PCR instrument.

The prepared PDMS was washed with anhydrous ethanol for 3 times, and the surface of the PDMS was treated by adding 20 μL anhydrous ethanol solution of MPS (2%, V/V) at room temperature for 0.5 h. After that, the excess solution was drained and washed with absolute ethanol and PBS (1 × , pH 7.4) for 3 times. The sulfhydryl group was successfully modified on the surface of PDMS channel. Finally, the reaction between the acrylamide groups on TDNs (0.1 μM, 20 μL) and the pendant thiol groups on the microchannels at room temperature for 2 h enabled TDNs to be successfully assembled on the substrate of PDMS through Michael addition (Liu et al., 2004).

2.3. Bacterial detection, in-microcavity bacterial culture and AST

E. coli O157: H7 cells were fluorescently labeled with SYTO9 Green (5 mM, 0.5 μL, 200 r min^{-1}, 37 °C for 30 min). 1 mL of each diluted sample of *E. coli* O157: H7 cell suspension (10^1–10^5 CFU/mL) was concentrated to 100 μL and injected into microchannels for 1 h at 37 °C. After washing twice with PBS (1 × , pH 7.4), bacteria cells were observed under a fluorescence microscope.

After the released *E. coli* O157: H7 cells and fresh LB medium entering the microcavities successively, the PDMS chip was placed in a water bath and incubated at 37 °C. The growth of bacteria was monitored under an optical microscope at 1-h intervals. Likewise, a series of antibiotics dilutions (0.125–32 μg mL^{-1}) were introduced into the microcavities for subsequent AST analysis.

3. Results and discussion

3.1. The working principle of the integrated microfluidic platform

The chip consists of six separate microchannels (Fig. 1A). Each microchannel consists of two parts: upstream and downstream microchannel (Fig. 1B). In the upstream channel, herringbone microstructures staggered periodically with each "mixing cycle" defined by two sequential groups of shifted chevrons (ten chevrons of each group) (Forbes and Kralj 2012; Lynn and Dandy 2007). The main function of upstream part is to specifically capture the bacteria. To improve the contact frequency of DNA probes, a TDN with three acrylamide labels at bottom vertexes is assembled on the substrate of the polydimethylsiloxane (PDMS) through Michael addition (Liu et al., 2004). On the other vertex, one DNA strand (poly T_{10}) stretches out with a biotin at the end. When streptavidin (SA) and biotin-aptamer (bio-Apt) (Kim et al., 2016) are added consecutively, biotin-Apts can be anchored onto the interface through biotin-streptavidin-biotin combination. When sample solution flows through the upstream channels, the bacteria will be specifically captured by the Apts on top of the TDNs (Fig. 1C). SYTO 9 green on bacteria generates a detectable fluorescence signal for quantification analysis.

The TDN in this work contains 13 base pairs in each edge which is about 4.42 nm long (Fig. 1D). TDNs provide rigid scaffolds with a height about 3 nm, thus increase the degree of freedom of the Apts and the contact frequence of the target bacteria. More importantly, TDN constructs an ordered plane arrangement with increased and consistent molecular distance (5.12×10^{12} TDNs per square centimeter, section *1.11* in SI). As a result, the recognizing and capturing capability can be obviously improved in comparison with traditional Apts which are single strands, tending to fold and collapse on the surface (Lin et al., 2015).

In the downstream channel, microcavities (100 μm in diameter) are uniformly distributed on both sides of the serpentine channel (35 μm in width) (Fig. 1E). The microcavities are connected with the main channels through narrow crossflow channels (35 μm in width). After the endonuclease interacts with the restriction sites on Apts (Sequence design about the site of EcoRI, section *1.12* in SI), bacteria captured at the aptsensing interfaces are released into microcavities, due to the hydrodynamic resistance principle (Zhu et al., 2014).

The red ink experiment (Fig. S1) clearly exhibited this enriching effect (Fig. 2A). Some red ink solution was added into the downstream channel until both serpentine channel and microcavities were filled (Fig. 2B). When the ink in serpentine channel was washed away, the microcavities remained filled with red ink under continuous negative pressure driving force (Fig. 2C). The result strongly demonstrated the feasibility of bacterial trapping in the microcavities, which laid the

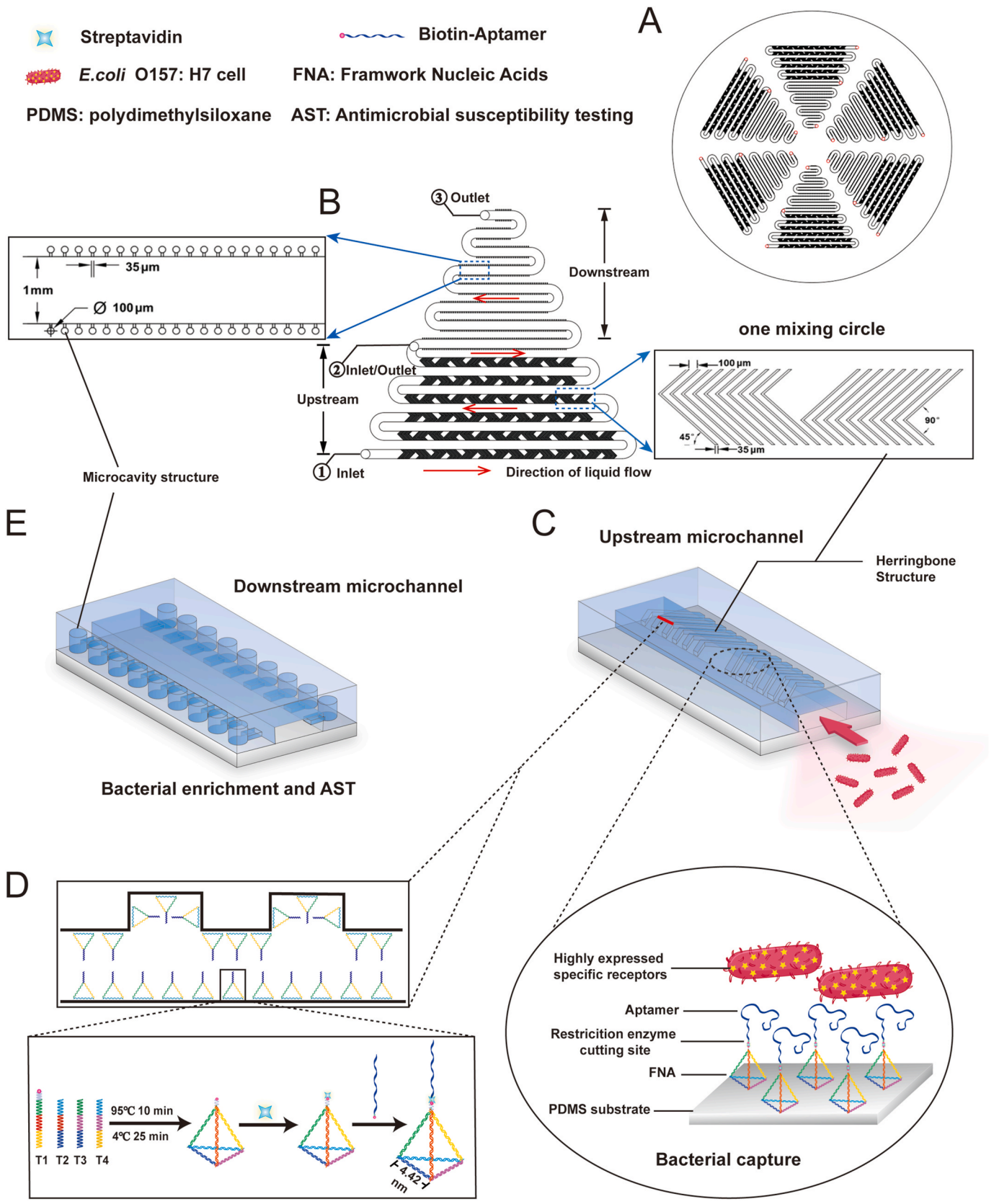

Fig. 1. Schematic illustration of the "one-stop" microfluidic platform for *E. coli* O157: H7. (A) Overall design diagram of the chip. (B) A single channel comprises herringbone structures (in upstream microchannels) and microcavities (in upstream microchannels). (C) 3D schematic of the herringbone structure and bacterial capture. (D) Fabrication of aptasensing interface and preparation of TDNs. (E) 3D schematic of the microcavity structures.

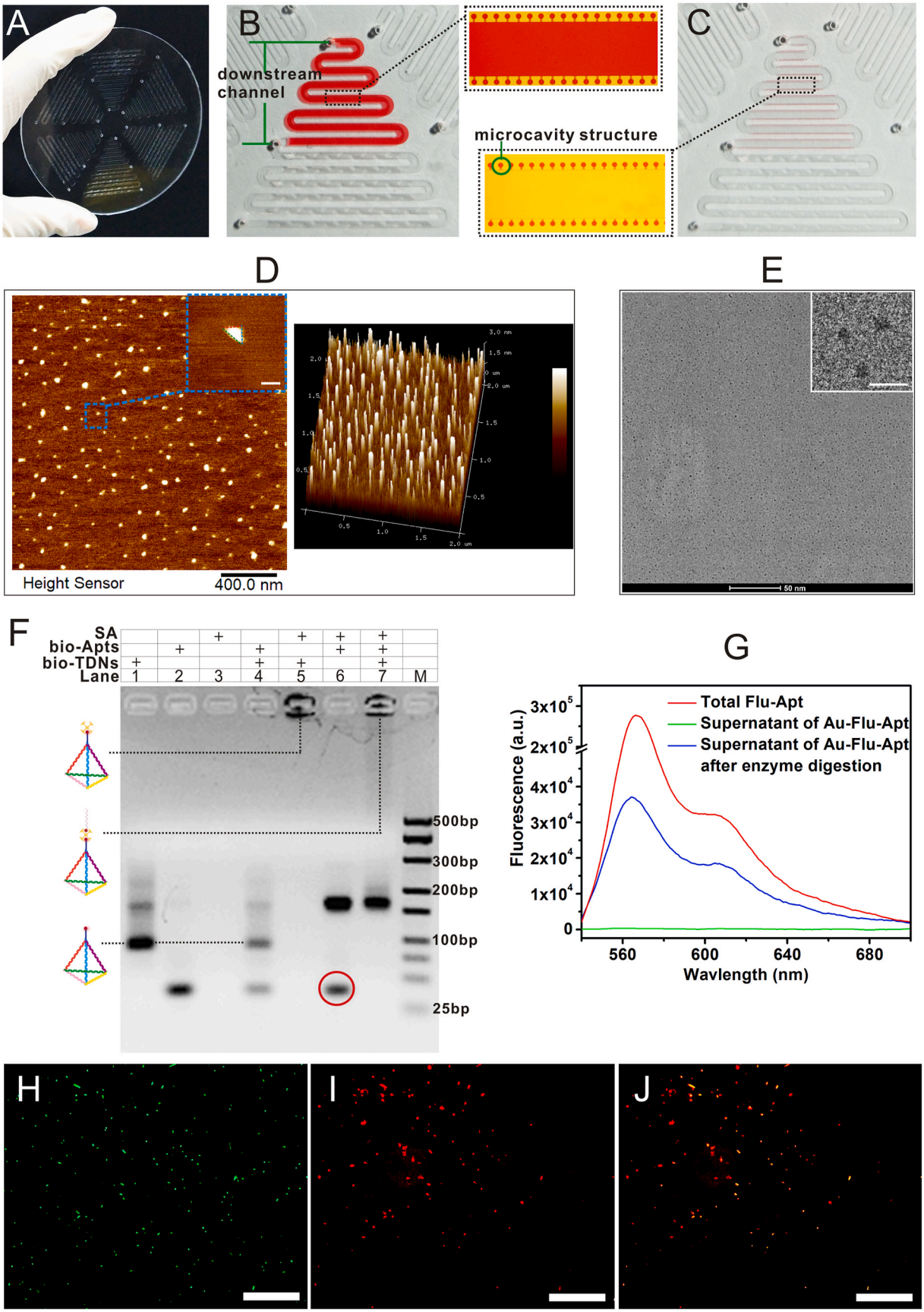

(caption on next page)

Fig. 2. (A) The microfluidic device developed in the work. (B) Red ink filled downstream microchannel completely. (C) Only microcavities were filled with red ink. (D) AFM illustration of TDNs. Top-view micrograph of 4 μm^2 scanning area (left) and the 3D image of height (right). Height bar was 3 nm. Insert: a high-magnification micrograph of TDN. The bar was 40 nm. (E) Cryo-TEM (Cryogenic Transmission electron microscope) characterization of TDNs. Insert: a high-magnification micrograph of TDN. The bar was 5 nm. (F) Agarose gel electrophoretic characterization of different complexes. Lane M: 25 bp DNA ladder Marker; Lane 1: bio-TDNs; Lane 2: bio-Apts; Lane 3: SA; Lane 4: bio-TDNs + bio-Apts; Lane 5: bio-TDNs + SA; Lane 6: bio-Apts + SA; and Lane 7: bio-TDNs + SA + bio-Apts. (G) Comparison of fluorescence values after enzyme restriction. (H) Fluorescence image of *E. coli* O157: H7 cells stained with SYTO green 9. (I) Fluorescence image of Cy3-labeled Apt/SA/TDNs complex on bacterial surface. (J) Overlap of the Figure H and I. Scale bars were 50 μm; the concentration of *E. coli* cells was 10^5 CFU mL^{-1}. (For interpretation of the references to color in this figure legend, the reader is referred to the Web version of this article.)

foundation for subsequent cell culture and AST.

The assembling of TDNs was demonstrated by using a Cy3 modified streptavidin (SA-Cy3). When TDNs with biotin and acrylamide labels were assembled and SA-Cy3 was added, significant fluorescence signal was produced (c1-c3, Fig. S2). However, when SA-Cy3 was added onto bare surface (a1-a3, Fig. S2) or TDN without acrylamide labels treated surface (b1-b3, Fig. S2), no obvious fluorescence signal was achieved. The results demonstrated the low unspecific absorption of the BSA-blocked microchannel surface.

3.2. Characterization of TDNs aptasensing interface

Formation of TDNs was firstly characterized using agarose gel electrophoresis. Right as expected, the TDN product showed distinct reduction in electrophoretic mobility after DNA molecular self-assembly (Fig. S3a). In addition, to further confirm the formation of the TDNs, we modified two strands of the TDNs (FT2 and FT4, Table S1, SI) with a pair of donor-acceptor dyes (cy3 and cy5) for fluorescence resonance energy transfer (FRET analysis) (Lin et al., 2015). As shown in Fig. S3b, the peak value of cy3 decreased at 570 nm, while that of cy5 increased at 670 nm, which resulted from the FRET because of the proximity of cy3 and cy5. This presence of FRET confirmed the successful formation of TDNs.

AFM images provided more direct evidence for the formation of TDNs, through top-view micrographs and 3D image of DNA nanostructures. As shown in Fig. 2D, a large number of independent nanostructures with a height of 3 nm appeared in the field of view in the experimental group. The contrast prepared with three DNA strands showed only flat chain-like products with a height of about 2 nm on the surface (Fig. S4a). And other AFM results also indicated that no 3-nm-high TDNs were successfully prepared (Fig. S4b-c). The high-magnification AFM graph and Cryo-TEM (Cryogenic Transmission electron microscope) characterization (Fig. 2E) indicated the triangular shape and good size uniformity of TDNs.

Then, the formation of TDNs-streptavidin-biotin aptamer (Apt/SA/TDNs) was investigated by electrophoresis. The results showed that the amount of the products increased when SA was increased, suggesting successful preparation of TDNs-SA compounds (Fig. S5). Then, the construction of the Apt/SA/TDNs complex was further characterized. As Fig. 2F showed, both TDNs/SA (lane 5) and SA/Apt (lane 6) had significantly reduced electrophoretic mobility compared with free molecules (lanes 1 and 2). Free biotin-Apts band (red circle in Fig. 2F) appeared in lane 6, but not in lane 7, because biotin-Apts combined with TDN/SA and thus stayed in the sample well.

3.3. Verification of enzyme restriction effect

Fluorescent characterization was performed to verify the restriction effect of the EcoRI on cleavage sites. An aptamer with one thiol and one fluorescence label at two ends (SH-Apt-Flu) was assembled onto the surface of Au nanoparticles (AuNPs). The supernatant of the last wash of the Au-Apt-Flu, with and without EcoRI, was analyzed. When EcoRI was added, the fluorescent signal of the supernatant dramatically improved (blue line, Fig. 2G), because the fluorescent probes were released into the solution after the phosphate diester bond was broken. In contrast, nearly negligible fluorescence signal was found without the restriction enzyme (green line, Fig. 2G). These results confirmed the capacity of bacterial release on the TDNs aptasensing interface.

3.4. Performance of TDNs aptasensing interface in E. coli O157: H7 detection

It has been reported that bacteria have good surface attachment (Tuson and Weibel 2013). So we took measures to block the surface of PDMS and reduce the adsorption behavior of bacteria on it (Fig. S6). The specific anchoring ability of Apt/SA/TDNs to *E. coli* O157: H7 was then demonstrated. Fluorescence imaging of SYTO 9 green-stained *E. coli* O157: H7 cells (Fig. 2H) and Cy3-labeled Apt/SA/TDNs complexes (Fig. 2I) was performed in the same field of view. The merged image (Fig. 2J) illustrated the positions of Cy3-Apt/SA/TDNs were consistent with the distribution of *E. coli* cells. These data clearly showed good specificity and capture capability of the aptasensing interface.

The detection sensitivity of the microfluidic platform was further verified through analysis of bacteria with concentration from 10^1 to 10^5 CFU mL^{-1}, in comparison with normal aptamer strategy. The results showed that the fluorescence signal of Apts/TDNs was always higher than that of normal aptamers at the same bacterial concentration (A and B in Fig. 3). It is worth noting that a single *E. coli* cell was visually observed by Apt/TDN at as low as 10^1 CFU mL^{-1} (red circle, Fig. 3A and Fig, S7a), while the regular aptamer strategy was only 10^3 CFU mL^{-1} (Fig. 3B and Fig. S7b). When we analyzed the relative fluorescence intensity of the image, the signal intensity of Apt/TDN was proved to be 35-fold higher than that of normal aptamer for 10^5 CFU mL^{-1} bacteria (Fig. 3C). A calibration curve was constructed in Fig. 3D ($Y = 0.73943X-0.08464$, $R^2 = 0.9986$) from 10^1 to 10^5 CFU mL^{-1}, spanning over 5 orders of magnitudes. The limit of detection was determined to be 10^1 CFU mL^{-1} experimentally (Calculation details can be found in section *1.11* in SI).

As mocking tests, different concentrations of *E. coli* O157: H7 were spiked into the blank milk samples (Zhang et al., 2020). The recoveries (Table S2) were from 93.5% to 107.1% with relative standard deviations (RSDs) of 2.6%–4.5% (<10%), indicating acceptable accuracy and precision of the Apt/TDNs-based biosensor for *E. coli* O157: H7.

The specificity of the TDNs-aptasensing method was also investigated. As shown in Fig. 3E, the fluorescence intensity induced by non-specific bacteria was negligible compared with that of specific *E. coli* O157: H7. Such partnership between Apts and TDNs set up an entity of capture interface, endowing this recognition means with extraordinary sensitivity and selectivity.

Noteworthily, double-labeling fluorescence analysis was realized in our system. After SYTO 9 green labeled bacteria were captured, Cy3 labeled Apts were added to combine onto the spare surface of *E. coli* O157: H7 (Fig. 3F). The results were shown in Fig. 3G: the left figure showed the SYTO 9 green on the genetic materials inside the bacteria, the middle figure showed red signal from Cy3-Apts on the surface, and the merged image clearly demonstrated that two signals came from different locations of the same bacteria. We believe the double-labeling analysis can effectively improve the specificity based on the analysis on two fluorescence channels, and the sensitivity can be further improved by applying rolling circle amplification (RCA) to these Apts primers (Yan et al., 2012).

3.5. Bacterial enrichment and culture

Distinct from the enrichment of immune magnetic beads, which requires a series of biochemical identification after cell culture, the

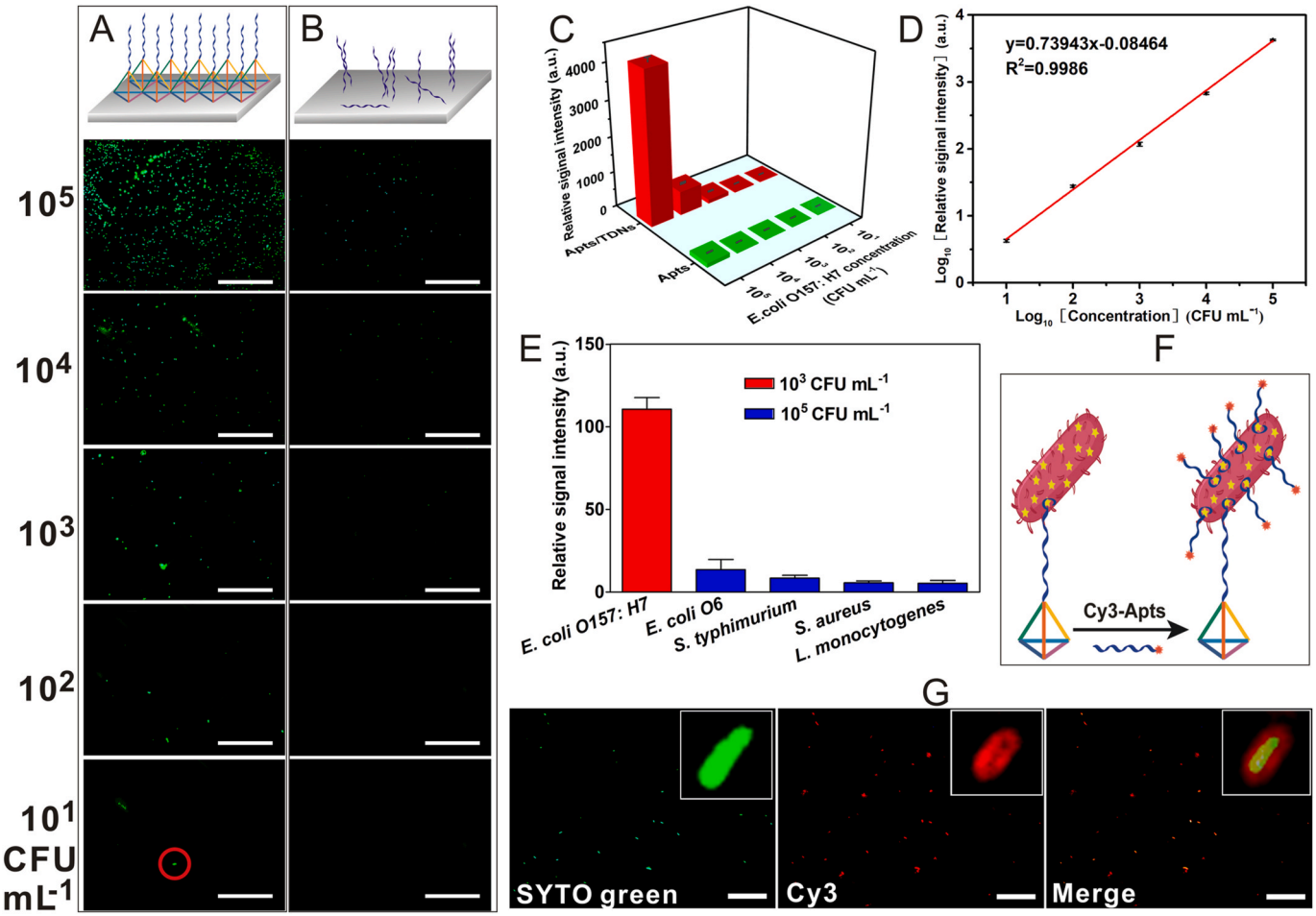

Fig. 3. Fluorescence images of *E. coli* O157: H7 cells captured by Apts/TDNs (A) and regular Apts (B); Bacteria cells were stained with SYTO green 9. (C) Comparison of relative fluorescence intensity between experimental groups (A) and control groups (B) at bacterial concentrations of 10^5–10^1 CFU mL^{-1}. (D) Calibration curve for the analysis of *E. coli* O157: H7 (each point represented 3 parallel experiments). (E) The specificity of the TDNs-aptasensing method. From left to right: *E. coli* O157: H7 cells (10^3 CFU mL^{-1}) and 10^5 CFU mL^{-1} of *E. coli* O6, *Salmonella typhimurium* (*S. typhimurium*), *Staphylococcus aureus* (*S. aureus*) and *Listeria monocytogenes* (*L. monocytogenes*), respectively. Scale bars were 50 μm. (F) Schematic diagram of the recognition between Cy3-Apts and free active sites on the surface of captured bacteria. (G) *E. coli* O157: H7 cells stained with SYTO green 9 (in green color), Cy3-Apts on the surface of captured bacteria (in red color), and the merged image. Insert: High-magnification micrograph of the bacterial cell. (For interpretation of the references to color in this figure legend, the reader is referred to the Web version of this article.)

invention here works in a microcavity structure to monitor the bacterial state in real time. Fig. 4A showed the optical and the corresponding fluorescent image of trapped *E. coli* O157: H7 (10^6 CFU mL^{-1}). As the concentration of *E. coli* cells decreased, the number of bacteria enriched in microcavities responsively decreased (Fig. S8). According to the statistical analysis, the enrichment rate of bacteria reached 92.8% (section *1.11* in SI). Then, the performance of microcavity as an individual bacterial culture chamber was verified. As shown in Fig. 4B, bacteria grew and dispersed in the circular space vigorously, until they crowded with each other and filled the microcavity. We compared the proliferation capacity of cells in microcavities with that of conventional 96-well method (Fig. 4C). Interestingly, although both methods reflected the proliferation of bacteria during the lag phase and logarithmic growth period, the growth efficiency in microcavities was obviously higher than that of traditional method (Fig. 4D) (Univariate Analysis of Variance in section *1.11* of SI), the result of which was consistent with previous literature (Luo et al., 2008). This results also strongly suggested that bacteria remained highly active after manipulations such as capture and release.

3.6. In-microcavity AST of E. coli O157: H7 cells

AST is essential for precise antibiotic delivery against antimicrobial resistance (AMR) (Doern 2011; Reller et al., 2009). However, the main problem with current AST methods is the speed, mainly due to the long lag phase and low growth rate of microorganisms (Bertrand 2019; van Belkum et al. 2019, 2020). It was clearly shown in Fig. 4D that the growth efficiency of bacteria in microcavities was obviously higher in the lag phase and logarithmic phase, thus we believe in-microcavity AST should be more effective. Moreover, our chip can further improve the experiment efficiency by using six serpentine microchannels for the study of varied changes of bacteria under the stimulation of different concentrations of antibiotics, or different kinds of antibiotics.

Therefore, as a proof-of-principle, *E. coli* O157: H7 captured by the upstream channels and released into downstream microcavities were taken as the model bacteria to verify the performance of in-microcavity AST strategy. From the four most common classes of antibiotics with different antibacterial mechanisms (Kapoor et al., 2017), six representative antibiotics were selected as follows: kanamycin sulfate (KS) and streptomycin sulfate (SS) are aminoglycosides; ofloxacin (OFX) and norfloxacin (NOR) are quinolones; chloramphenicol (CHL) belongs to chloramphenicol and lincomycin hydrochloride (MY) is a lincosamide.

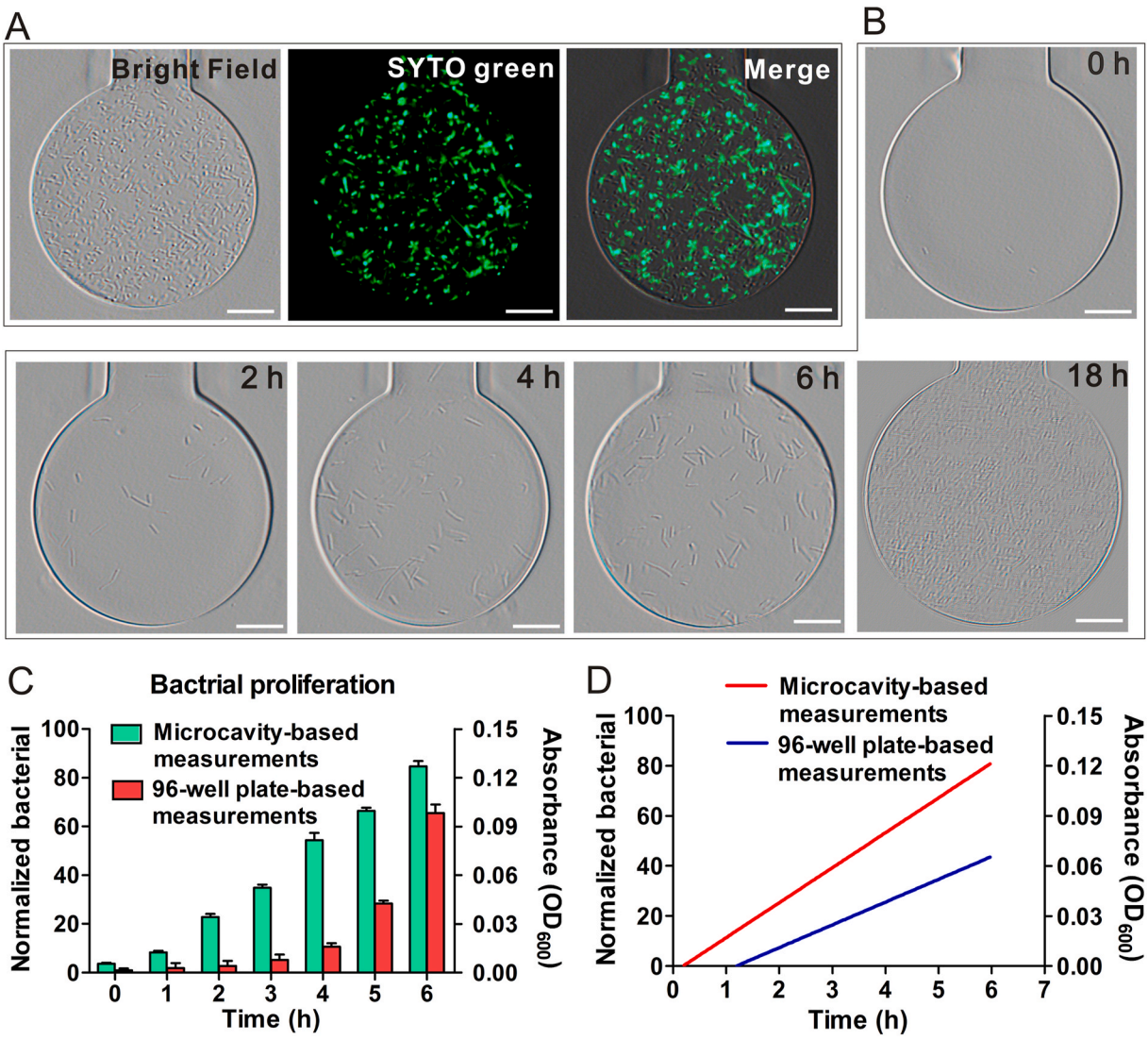

Fig. 4. (A) Optical image, fluorescence image and merged image of cells enriched in microcavities from left to right. The initial bacteria concentration was 10^6 CFU mL^{-1}. (B) Optical images of the proliferation of *E. coli* O157: H7 cells (with an initial concentration of 10^2 CFU mL^{-1}) in microcavities over time from 0 h to 18 h. Scale bars were 20 μm. (C) Comparison of proliferation results of *E. coli* O157: H7 cells in microcavities and 96-well plates with equal culture time. (D) Univariate analysis of variance between the proliferation in microcavities and in 96-well plates.

It has been now widely accepted that aminoglycosides, quinolones, and chloramphenicol belong to broad-spectrum antibiotics which can effectively kill a variety of bacteria or slow their growth; lincosamide antibiotics have a more significant biasing activity against most of the Gram-positive bacteria. On this basis, we assumed that the number of *E. coli* O157: H7 in microcavities should decrease when exposed to KS, SS, OFX, and NOR, as well as CHL, while MY should have no significant effect on it. The results in Fig. 5 were just as expected. Each of the time-killing and dose-response graphs from Fig. 5A–E showed clear antimicrobial effect of the corresponding antibiotic. For MY, there was no significant antibacterial effect even at the concentrations of 8 μg mL^{-1} (Fig. 5F). The minimum inhibitory concentration (MIC) is defined as the lowest concentration of a drug that inhibits the visible growth of a microorganism (Lee et al., 2019). The MICs of KS, SS, OFX, NOR, and CHL were 4, 8, 0.5, 1, and 2 μg mL^{-1} respectively. We also found that though MY was less effective against Gram-negative bacteria, it still showed antibacterial activity against *E. coli* O157: H7 at higher concentrations (Fig. S9).

These results were consistent with broth dilution method performed in 96-well plates (Fig. S10), demonstrating the efficacy of in-microcavity AST strategy. Not only that, in-microcavity strategy benefited AST in two other aspects: First, its time-consuming was greatly reduced. In-microcavity AST can be completed in 5 h, while the traditional methods take at least 24 h. In addition, real-time study of drug resistant response was performed in microcavities, where the number and the morphological changes of bacteria can be visually observed. As shown in Fig. 5G and Fig. S11, with increasing KS concentration, we could intuitively monitor the decrease of *E. coli* population, and even observed fragments of dead bacteria (4 μg mL^{-1}, Fig. 5G). This real-time observation helps to identify individual cells that remain alive or in a state of suspended animation in the presence of antimicrobials, which may cause infection once more (van Belkum et al., 2020).

To exemplify the competency of the TDNs-based microfluidic platform in pathogen studying, a crosswise comparison was carried out among common available technologies in Table 1. This microfluidic platform served predominantly as an integrated device over other methods.

4. Conclusions

In summary, a “one-stop” microfluidic platform was developed by manipulating the elements of TDNs aptasensing interface in the fluidic

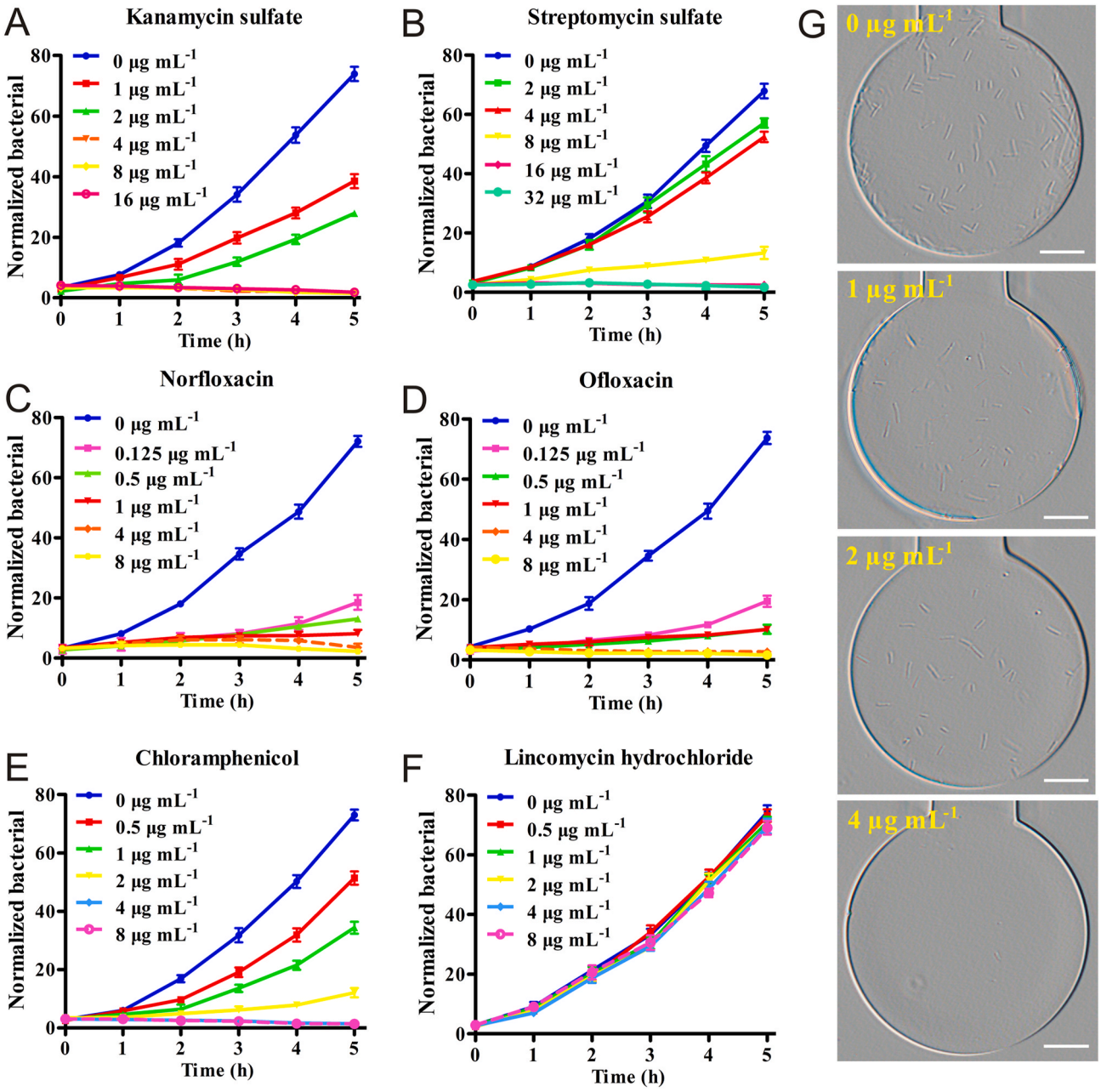

Fig. 5. (A–F) Time-lapse monitoring of bacterial susceptibility to the linearized concentration of six different antibiotics in the time-kill or the dose-response experiments. Measurements obtained from ten sets were averaged, and the experiments were replicated five times. The initial concentration of all the bacteria was 10^4 CFU mL^{-1}. (G) Optical images of bacteria in microcavities after 5 h of KS action. Scale bars were 20 μm.

system. The integration of essential components responds to simplified requirement for on-chip sized-based bacterial capture, release, enrichment, in-vitro culture and drug sensitive test. Compared with the existing methods, the integrated platform offers the following multiple unique advantages: (1) the spatial orientation of tetrahedral FNAs offers a nano-bio interface for fluidic microsystems, thus achieving a desirable molecular recognition efficiency; (2) the Apt/TDNs aptasensing interface serves as a chemical filter to selectively load target bacterial pathogens into the observation area. Therefore, it is not necessary to distinguish symbiotic bacteria from pathogens in complex samples and (3) bacterial inhibition in the microcavity can be observed visually in as little as 2 h. As a matter of fact, if the same fast AST is carried out on 96-well plates, false-positive results may be generated due to the vague absorption value at OD_{600}. In addition, the platform still needs to be further improved in several aspects, such as integrating automatic imaging analysis technology to improve the efficiency of signal collection, so as to meet the research needs of more actual samples in the future. All in all, this potent fusion across microfluidics and FNAs would chart a promising and invigorating course towards the future studies of pathogenic microorganism or tumor cells.

CRediT authorship contribution statement

Fulin Zhu: Conceptualization, Investigation, Writing - original draft. **Xiaojun Bian:** Data curation, Investigation. **Hongcai Zhang:** Validation. **Yanli Wen:** Data curation, Investigation. **Qian Chen:** Methodology. **Yongliang Yan:** Data curation. **Liang Li:** Validation, Supervision. **Gang Liu:** Writing - review & editing. **Juan Yan:** Writing - review & editing, Supervision.

Table 1
Comparison between the integrated microfluidic platform and the present methods.

Method	Functionality	Sample volume (μL)	Analysis Time	LOD (CFU mL^{-1})	Specificity	Cost	Ref.
Microbiological culturing and isolation	Culture AST	_	7–8 day	_	Low	Low	Velusamy et al. (2010)
ELISA	Detection AST	_	24 h	10^4	Low	High	Patel et al. (2020)
Multiplex PCR	Detection	100–200	3 h–4 h	3–200	High	High	Czilwik et al. (2015)
Aptamer-based colorimetric biosensor	Detection	_	>4 h	10^3	High	Low	Bayrac et al. (2017)
Raman spectroscopy	AST	100	2–3 h	_	_	High	Kirchhoff et al. (2018)
Microfluidics for bacterial movements	AST	<500	105 min-24 h	_	_	Low	Kara et al. (2018)
Dendrimer-aptamer-based microfluidics and RCA	Detection	50	>5 h	10^2	High	Low	Jiang et al. (2017)
Adaptable Microfluidic system	Classification Culture AST	20	30–120 min	5×10^3	Low	Low	Li et al. (2019)
Multi-layered centrifugal microfluidics	AST	200	3 h	_	_	High	Tang et al. (2018)
FNA-based Integrated microfluidic platform	Detection Release Enrichment Culture AST	<20	4–8 h	10^1	High	Low	This method

Declaration of competing interest

The authors declare that they have no known competing financial interests or personal relationships that could have appeared to influence the work reported in this paper.

Acknowledgements

This work was supported by the National Natural Science Foundation of China (Nos. 21775102, 21775104), Natural Science Foundation of Shanghai Municipal (Nos. 20ZR1424100, 19ZR1422900), the Agricultural Science and Technology Innovation Program of CAAS (No. CAAS-ZDRW202009) and the National Quality Infrastructure Program of China (No. 2018YFF0212800).

Appendix A. Supplementary data

Supplementary data to this article can be found online at https://doi.org/10.1016/j.bios.2020.112943.

References

Bayrac, C., Eyidogan, F., Avni Oktem, H., 2017. Biosens. Bioelectron. 98, 22–28.
Bertrand, R.L., 2019. J. Bacteriol. 201, e00697, 00618.
Bush, K., Courvalin, P., Dantas, G., Davies, J., Eisenstein, B., Huovinen, P., Jacoby, G.A., Kishony, R., Kreiswirth, B.N., Kutter, E., Lerner, S.A., Levy, S., Lewis, K., Lomovskaya, O., Miller, J.H., Mobashery, S., Piddock, L.J., Projan, S., Thomas, C.M., Tomasz, A., Tulkens, P.M., Walsh, T.R., Watson, J.D., Witkowski, J., Witte, W., Wright, G., Yeh, P., Zgurskaya, H.I., 2011. Nat. Rev. Microbiol. 9, 894–896.
Czilwik, G., Messinger, T., Strohmeier, O., Wadle, S., von Stetten, F., Paust, N., Roth, G., Zengerle, R., Saarinen, P., Niittymaki, J., McAllister, K., Sheils, O., O'Leary, J., Mark, D., 2015. Lab Chip 15, 3749–3759.
Dittrich, P.S., Tachikawa, K., Manz, A., 2006. Anal. Chem. 78, 3887–3908.
Doern, G.V., 2011. J. Clin. Microbiol. 49, S4.
Foley, J.O., Mashadi-Hossein, A., Fu, E., Finlayson, B.A., Yager, P., 2008. Lab Chip 8, 557–564.
Forbes, T.P., Kralj, J.G., 2012. Lab Chip 12, 2634–2637.
Ge, Z., Gu, H., Li, Q., Fan, C., 2018. J. Am. Chem. Soc. 140, 17808–17819.
Ge, Z., Li, Q., Fan, C., 2020. Chem. Res. Chin. Univ. 36, 1–9.
Helmke, B.P., Minerick, A.R., 2006. Proc. Natl. Acad. Sci. U.S.A. 103, 6419–6424.
Hermann, C.A., Duerkop, A., Baeumner, A.J., 2019. Anal. Chem. 91, 569–587.
Jiang, Y., Zou, S., Cao, X., 2017. Sensor. Actuator. B Chem. 251, 976–984.
Jones, C.H., Hakansson, A.P., Pfeifer, B.A., 2014. J. Mater. Chem. B 46, 8053–8068.
Kapoor, G., Saigal, S., Elongavan, A., 2017. J. Anaesthesiol. Clin. Pharmacol. 33, 300–305.
Kara, V., Duan, C., Gupta, K., Kurosawa, S., Stearns-Kurosawa, D.J., Ekinci, K.L., 2018. Lab Chip 18, 743–753.
Kim, Y.S., Raston, N.H., Gu, M.B., 2016. Biosens. Bioelectron. 76, 2–19.
Kirchhoff, J., Glaser, U., Bohnert, J.A., Pletz, M.W., Popp, J., Neugebauer, U., 2018. Anal. Chem. 90, 1811–1818.
Lee, W.B., Chien, C.C., You, H.L., Kuo, F.C., Lee, M.S., Lee, G.B., 2019. Lab Chip 19, 2699–2708.
Li, H., Torab, P., Mach, K.E., Surrette, C., England, M.R., Craft, D.W., Thomas, N.J., Liao, J.C., Puleo, C., Wong, P.K., 2019. Proc. Natl. Acad. Sci. U.S.A. 116, 10270–10279.
Li, S., Ma, Z., Cao, Z., Pan, L., Shi, Y., 2020. Small 16, e1903822.
Li, Z., Wei, B., Nangreave, J., Lin, C., Liu, Y., Mi, Y., Yan, H., 2009. J. Am. Chem. Soc. 131, 13093–13098.
Lin, M., Wang, J., Zhou, G., Wang, J., Wu, N., Lu, J., Gao, J., Chen, X., Shi, J., Zuo, X., Fan, C., 2015. Angew Chem. Int. Ed. Engl. 54, 2151–2155.
Liu, D., Perdue, R.K., Sun, L., Crooks, R.M., 2004. Langmuir 20, 5905–5910.
Liu, N., Zhang, X., Li, N., Zhou, M., Zhang, T., Li, S., Cai, X., Ji, P., Lin, Y., 2019. Small 15, e1901907.
Liu, Z., Banaei, N., Ren, K., 2017. Trends Biotechnol. 35, 1129–1139.
Luo, W., Jones, S.R., Yousaf, M.N., 2008. Langmuir 24, 12129–12133.
Lynn, N.S., Dandy, D.S., 2007. Lab Chip 7, 580–587.
Ozen, M.O., Sridhar, K., Ogut, M.G., Shanmugam, A., Avadhani, A.S., Kobayashi, Y., Wu, J.C., Haddad, F., Demirci, U., 2020. Biosens. Bioelectron. 150, 111930.
Patel, J., Yin, H.B., Bauchan, G., Mowery, J., 2020. Food Microbiol. 86, 103303.
Qu, X., Yang, F., Chen, H., Li, J., Zhang, H., Zhang, G., Li, L., Wang, L., Song, S., Tian, Y., Pei, H., 2017. ACS Appl. Mater. Interfaces 9, 16026–16034.
Rajapaksha, P., Elbourne, A., Gangadoo, S., Brown, R., Cozzolino, D., Chapman, J., 2019. Analyst 144, 396–411.
Reller, L.B., Weinstein, M., Jorgensen, J.H., Ferraro, M.J., 2009. Clin. Infect. Dis. 49, 1749–1755.
Shin, D.J., Andini, N., Hsieh, K., Yang, S., Wang, T.-H., 2019. Annu. Rev. Anal. Chem. 12, 41–67.
Song, P., Shen, J., Ye, D., Dong, B., Wang, F., Pei, H., Wang, J., Shi, J., Wang, L., Xue, W., Huang, Y., Huang, G., Zuo, X., Fan, C., 2020. Nat. Commun. 11, 838.
Stroock, A.D., Dertinger, S.K., Ajdari, A., Mezic, I., Stone, H.A., Whitesides, G.M., 2002. Science 295, 647–651.
Su, Y., Li, D., Liu, B., Xiao, M., Wang, F., Li, L., Zhang, X., Pei, H., 2019. ChemPlusChem 84, 512–523.
Tang, M., Huang, X., Chu, Q., Ning, X., Wang, Y., Kong, S.K., Zhang, X., Wang, G., Ho, H. P., 2018. Lab Chip 18, 1452–1460.
Tuson, H.H., Weibel, D.B., 2013. Soft Matter 9, 4368–4380.
van Belkum, A., Bachmann, T.T., Lüdke, G., Lisby, J.G., Kahlmeter, G., Mohess, A., Becker, K., Hays, J.P., Woodford, N., Mitsakakis, K., Moran-Gilad, J., Vila, J., Peter, H., Rex, J.H., Dunne, W.M., 2019. The, JPIAMR AMR-.RDT working group on antimicrobial resistance and rapid diagnostic testing. Nat. Rev. Microbiol. 17, 51–62.
van Belkum, A., Burnham, C.-A.D., Rossen, J.W.A., Mallard, F., Rochas, O., Dunne, W.M., 2020. Nat. Rev. Microbiol. 18, 299–311.
Velusamy, V., Arshak, K., Korostynska, O., Oliwa, K., Adley, C., 2010. Biotechnol. Adv. 28, 232–254.
Wang, W., Yu, S., Huang, S., Bi, S., Han, H., Zhang, J.R., Lu, Y., Zhu, J.J., 2019. Chem. Soc. Rev. 48, 4892–4920.
Whitesides, G.M., 2006. Nature 442, 368–373.
Williams, M.S., Longmuir, K.J., Yager, P., 2008. Lab Chip 8, 1121–1129.
Wiraja, C., Zhu, Y., Lio, D.C.S., Yeo, D.C., Xie, M., Fang, W., Li, Q., Zheng, M., Van Steensel, M., Wang, L., Fan, C., Xu, C., 2019. Nat. Commun. 10, 1147.
Xu, B., Du, Y., Lin, J., Qi, M., Shu, B., Wen, X., Liang, G., Chen, B., Liu, D., 2016. Anal. Chem. 88, 11593–11600.
Yan, J., Su, S., He, S., He, Y., Zhao, B., Wang, D., Zhang, H., Huang, Q., Song, S., Fan, C., 2012. Anal. Chem. 84, 9139–9145.
Yang, F., Li, Q., Wang, L., Zhang, G.-J., Fan, C., 2018a. ACS Sens. 3, 903–919.

Yang, F., Zuo, X., Fan, C., Zhang, X.-E., 2018b. Natl. Sci. Rev. 5, 740–755.
Zhang, J., Jiang, Y., Xia, X., Wu, J., Almeida, R., Eda, S., Qi, H., 2020. Biosens. Bioelectron. 165, 112366.
Zhu, Q., Qiu, L., Yu, B., Xu, Y., Gao, Y., Pan, T., Tian, Q., Song, Q., Jin, W., Jin, Q., Mu, Y., 2014. Lab Chip 14, 1176–1185.